Sponsored Research Project
The Autonomous Digital Power Grid (GridX)
Center of Excellence for NEOM Research at KAUST

Phase II Project Report

Grid Modeling and Computer System Technologies for AI/ML-based Microgrid Controls

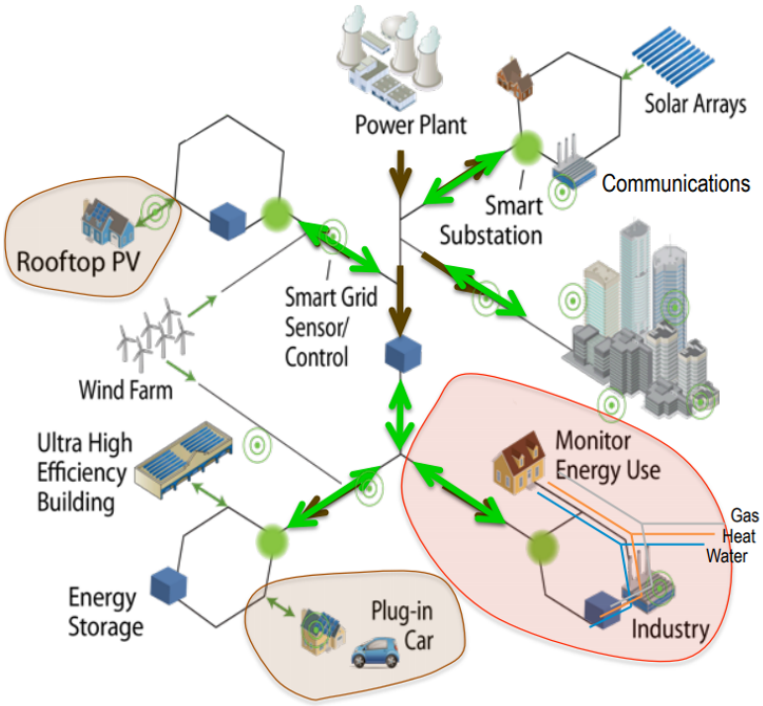

Principal Investigator: Prof. Luigi Vanfretti
Research Assistants: Shunyao Xu, Justin Johnson, Hayleigh Sanders
Project Manager: Dr. Hamed Nademi

October 8th, 2020

ALSETLab Research Group
Electrical, Computer & Systems Department
Rensselaer Polytechnic Institute, Troy, NY

Table of Contents

1. Abstract

The main scope of this report is to give an update on RPI work progress for Phase II of the project, mainly referred to WP1, WP2 and partly WP3 and WP4.

This report discussed the development of two models, microgrid model and Wind Farm based on Type 3 turbines through MATLAB/Simulink using Switching equivalent circuits for power electronic components. Comparative analysis of the obtained results is included for developed models.

Benchmarking of ML hardware platforms was conducted using an NVIDIA Jetson, NVIDIA TX2, Google Coral Development board, Google Edge TPU USB Accelerator, and Raspberry Pi, and the results obtained from this benchmarking are also included in this report.

Sensing and data acquisition requirements were derived by implementing two data acquisition modules and evaluating the impact of the data acquisition modules under different input signals. Here, the effects of different ADC resolutions on accuracy of the results are compared in terms of computational burden utilizing the custom-built data acquisition boards.

Energy storage modeling and analysis for implementation on RT simulators such as OPAL-RT and Typhoon HIL are also discussed in this document. These models provide a simplified equivalent circuit-based model of the inner workings of the battery. The goal is to exploit these models together with the models of the battery converters developed in Chapter 1, so that the battery can be utilized as an actuator for different control functions, for example, to counter the oscillations from a wind-farm or to balance the output of a PV.

2.2. Terms and Definitions

Terms/abbreviation	Definition
ADC	Analog-to-Digital Converter
BESS	Battery Energy Storage System
CHIL	Controller Hardware-in-the-loop
DER	Distributed Energy Resource
DFIG	Doubly Fed Induction Generator
DG	Diesel Generator
DOL Motor	Direct On Line Motor
EMT	Electromagnetic Transient
EUT	Equipment Under Test
FMU	Functional Mock-up Unit
FPGA	Field Programmable Gate Array
GSC	Grid Side Power Converter
HIL	Hardware-In-the-Loop
LI-ion	Lithium ion
ML	Machine Learning
PCC	Point of Common Coupling
PV	Photovoltaic
PWM	Pulse Width Modulation
RSC	Rotor Side Power Converter
RT simulation	Real-Time simulation
SSCI	Sub-synchronous Control Interaction
SSR	Sub-synchronous Resonance
VSC	Voltage Source Converter
VSD Motor	Variable Speed Drive Motor
WP	Work Package

3. WP1- Microgrid Model Developments

This chapter gives an overview of the method and procedure to develop system models and corresponding responses in both the normal operating condition and transients by numerical simulation.

3.1 General Considerations for Simulated Models

The semiconductor power devices comprising power converters, e.g., PV inverters, such as IGBTs, MOSFETs and diodes, are typically modeled as ideal switches in power system EMT simulation. A voltage source with its impedance model is considered to represent an AC grid in addition to the PQ model for equivalent load/consumers connected to the PCC. The modeling of loads as PQ is useful as a worst-case conservative assumption, and can also be wisely applied in mid-term dynamic simulation. This report describes works under consideration based on the two models implemented using MATLAB/ Simulink. A typical control schemes for designing all subsystems forming the entire microgrid are presented.

In recent years, IEEE released a Technical Report entitled “Microgrid Stability Definitions, Analysis, and Modeling” [3] with the purpose of educating and establishing standards for researchers into the subject. In today's grid configuration, Microgrids have become of utmost importance for electrical power research and studies due to the bidirectionality of power flux, islanded operation, dynamics decoupling in a significant presence of Distributed Energy Resources (DER’s). Although the backbone of energy distribution still is, and will probably be for the next decades, a centralized energy facility with ramifications that reach consumers, DER’s such as Wind, Photovoltaic, and energy storages are challenging the way we study the grid.

In order to study the impact of Load Dynamics and its various effects, IEEE has a microgrid test system depicted in Fig. 1, that can be used in the project. There are three different operating scenarios will be addressed in the study: Islanded Operation, Reconnection, and Active Power balancing with battery usage.

3.1.1 IEEE Microgrid Test Model in MATLAB/Simulink

The microgrid system developed in Typhoon software employed for initial system analysis and
The IEEE microgrid test system from [3] is developed in the Simulink environment for system analysis and acquiring measurement data to set up and train Neural Network models. Fig. 2 shows the employed study system comprising PV source, Battery storage, Diesel Generator and AC Grid. Initially, the microgrid is operated in grid-connected mode, but does not exchange

active power with the main grid. The solar PV system generates 35 kW, the diesel generator generates 20 kW, and the battery energy storage system injects 5.5 kW to maintain the power balance in the microgrid. The simulation system is specified with the given rating values in Table 1.

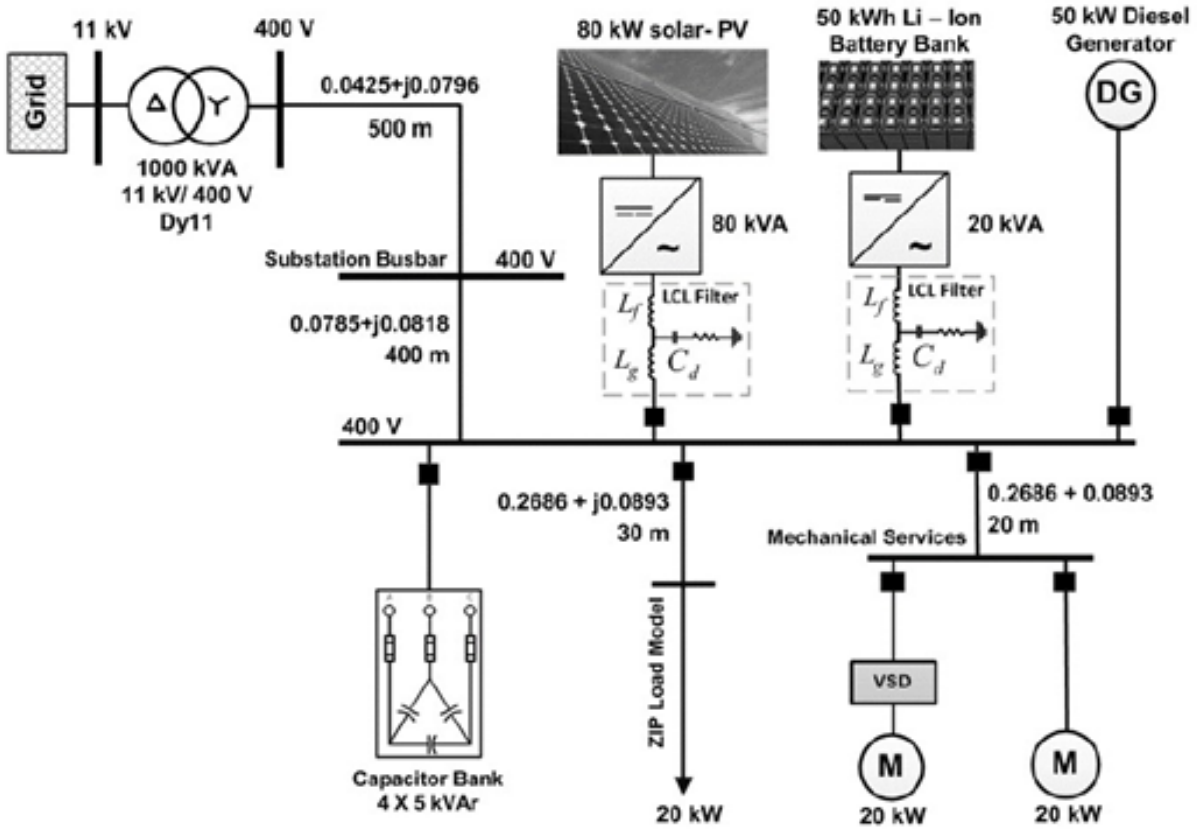

Figure 1 - IEEE Microgrid Test System for Dynamic and Stability Studies

Common 400V busbar interconnected to the common point of coupling feeding from grid transformer is supplying different load types (e.g., Variable loads, DOL motor loads, VSD motor loads), which makes up a total load of 60 kW, with each load type having equal capacity, i.e., 20 kW. The variable load is represented by a residential load model varying from 15 kW to 25 kW. The DOL motor load is represented by a fan load (Induction motor), and the VSD motor load with space vector modulation is represented by a pump load.

This model is useful to investigate the importance of the load characteristics and its effects for microgrid stability.

TABLE 1: Rating Values and Parameters for the IEEE Microgrid Model

Parameters	Value	Parameters	Value
VSD / DOL Motor Rating	20kW	LI-ion Battery Capacity	50kWh
PV Inverter Power	80kVA	Diesel Generator Power	50kW
Busbar Voltage	400V	Variable Load Capacity	15kW-25kW
Grid Transformer Ratio	11kV / 400V	Battery Inverter Power	20kVA

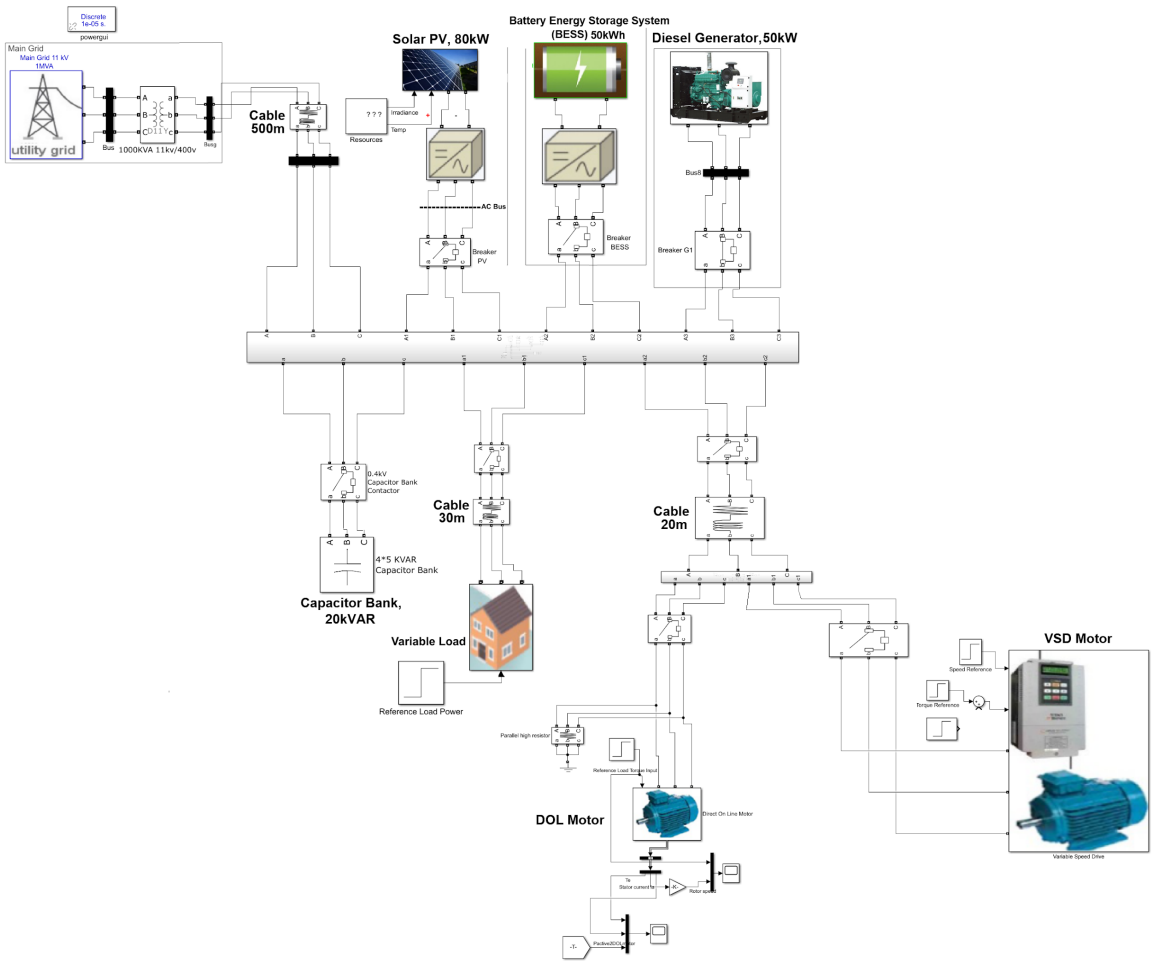

Figure 2 - Configuration of IEEE microgrid test case in Simulink used for applying ML techniques.

3.1.1.1 Battery Energy Storage Conversions

Energy Storage is an increasing trend for many applications including microgrids, where it can be used for propulsion in transportation era or can optimize the load situation by delivering or consuming power from the grid, it is not an energy source, meaning that over time it must always consume as much energy as it delivers.

There are many different technologies that can be used as energy storage for electrical power systems, including batteries, capacitors, hydrogen fuel cells, flywheels or superconducting magnetic ES. Batteries have the advantage of having high energy density. They also keep an almost constant voltage. Capacitors as energy storage can handle much bigger currents than a battery, and is therefore said to have higher power density. But the limited energy density of the capacitors means that they will take up a lot of space. They also discharge fast, which may make them unsuitable for back up energy reserve in case of generation blackout. Batteries could potentially be connected directly to the DC bus in Fig. 3, but this will set limits for the operating voltage of the system. A bidirectional DC-DC converter offers more flexibility to the system and makes it easier to control the energy flow to and from the battery.

The most commonly available inverters for PV and Battery energy storage are based in two blocks: a DC-DC converter and a DC-AC converter (Fig. 3) [4, 5]. The former converter increases the voltage and performs the MPP tracking in case of PV application, while the latter generates the sinusoidal output current by means of a PWM modulation. However, there have been several reported designs in which the converter topology is a single-stage DC-AC converter that performs both the MPP tracking and the sinusoidal current waveform generation.

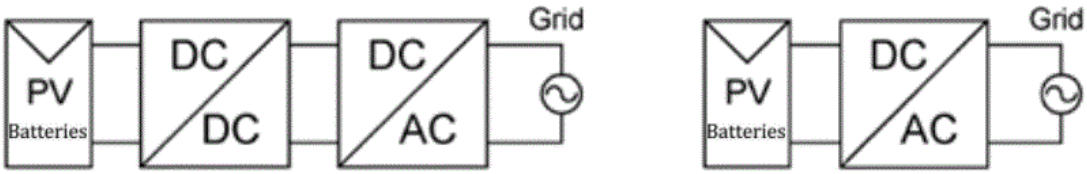

(a) (b)

Figure 3 - Different power converter structures for PV and Battery energy storage: (a) multi-stage converter and (b) single-stage power converter.

The modelled chopper is a DC-DC bidirectional converter illustrated in Fig. 4. The four power switches are modelled as IGBT switches with freewheeling diodes. This means that the model can be extended to include switching losses and Snubber circuits for the switches in the model. The diodes have a forward voltage of 0.8V which is a typical value for most power diodes [6].

The inductor can either be a transformer or a coil with an iron core, but it is modelled as an ideal inductor. Below equation shows how minimum inductor size can be calculated for boost and buck converters, assuming continuous conduction mode and lossless converter. This equation

can be used to approximate minimum inductor size for a known frequency and acceptable current ripple. A big inductor will take up space and weigh, but will allow higher switching frequency.

$$L_{min} = \frac{V_{LV}(V_{HV} - V_{LV})}{f_s \cdot \Delta I_L \cdot V_{HV}}$$

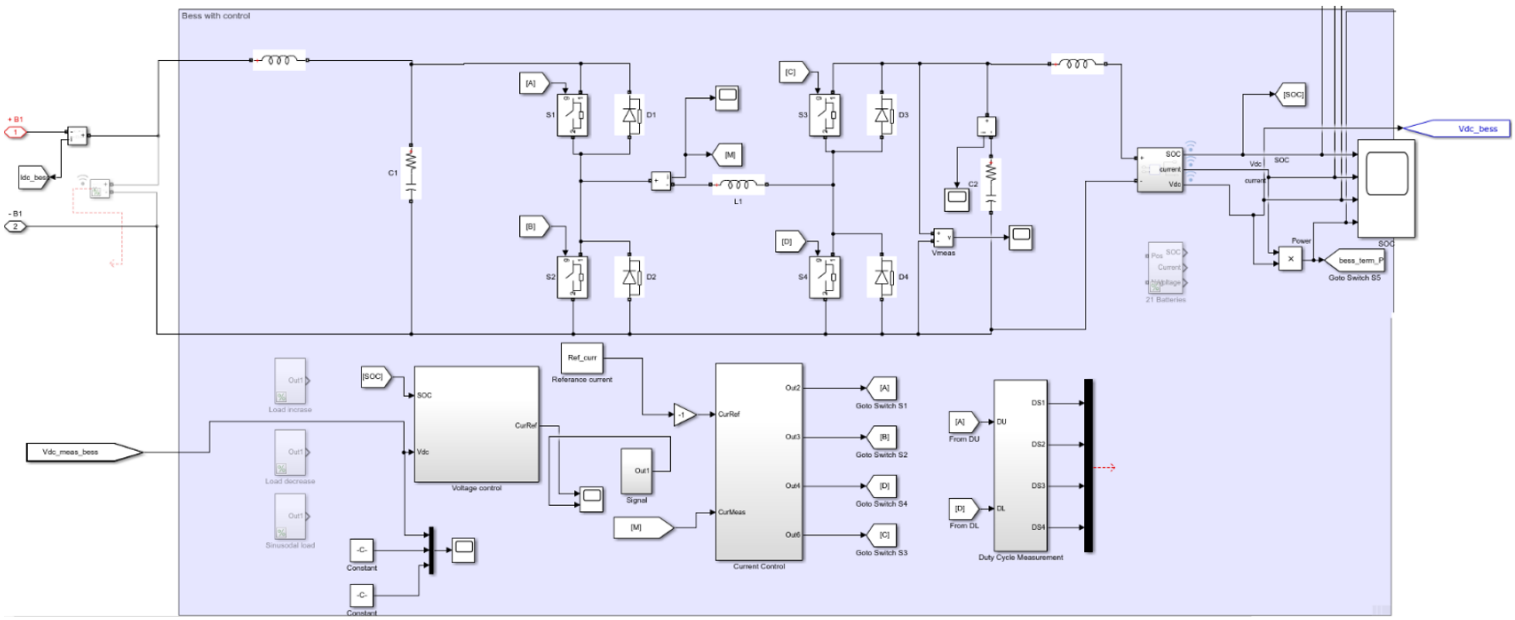

Figure 4 - BESS Bidirectional DC-DC converter and its control

Switching frequency for the converter is typically from 2kHz-5kHz. Higher switching frequency will give higher switching losses. For this model the frequency is set to 5 kHz, and the inductor is set to 40 mH, but the model is made such that parameters can easily be changed and experimented with intended application requirements.

Capacitor banks are modelled as ideal capacitors with a resistor in series. Capacitors decide the voltage ripple. The resistor represents the internal resistance of the capacitor.
As depicted in Fig. 4, the DC bus is modelled as a controlled voltage source with an inductor in series. The inductance of the bus is set to 387 μH, which is a typical value based on experience. In a real system, this inductance will depend on the rating of the bus, topology and configuration of generation resources, conversion topology and loads. Circuit parameters used in the model are given in Table 2.

TABLE 2: Circuit parameters for used DC-DC converter model

L1	40 mH
C1, C2	3mF
RC1, RC2	0.02 Ω
Switching frequency	5kHz
Bus inductance, L2, L3	387 μH

The battery module made up of single battery pack or consists of 21 batteries in series. Simulink has a built-in battery model, where battery characteristics are calculated based on a few input parameters and typical values for the given battery type. Data for the batteries is based on the datasheet available in [7] for Corvus AT6500 lithium batteries. Parameters for one battery are displayed in Table 3, and the Voltage-Capacity characteristics are depicted in Fig. 5.

The battery has a maximum charge current of 350A and maximum discharge current of 598A, restricted by the chemical processes in the battery. But to avoid overheating, the maximum continuous current is 120 A. As seen from battery characteristic curves in Fig. 5, the voltage of each battery will be between 45V and 50V under normal operation. This means that with 21 batteries in series, the voltage will vary between 924 and 1050 volt if the state-of-charge (SOC) is maintained over 60%. With a nominal DC voltage of 930V, which side of the converter with the highest voltage will vary.
To make a model for 21 batteries in series, one can either connect 21 44V-batteries in series or use one battery with nominal voltage of 932V.

Control strategy implemented for Battery Module

a) Current Control Strategy

There are two levels of control for the battery and DC-DC converter. The current control decides the duty cycle for each of the power switches based on a current reference and current measurement. The switching logics for the current control are shown in Fig. 6 while the control signal is compared with two triangular signals. The upper triangular signal decides the duty cycle for switch S1 and S2 (see Fig. 4) while the lower triangular signal decides duty cycle for switch S3 and S4. The gate signals for S1 and S2 are always opposite, the same sends to S3 and S4.

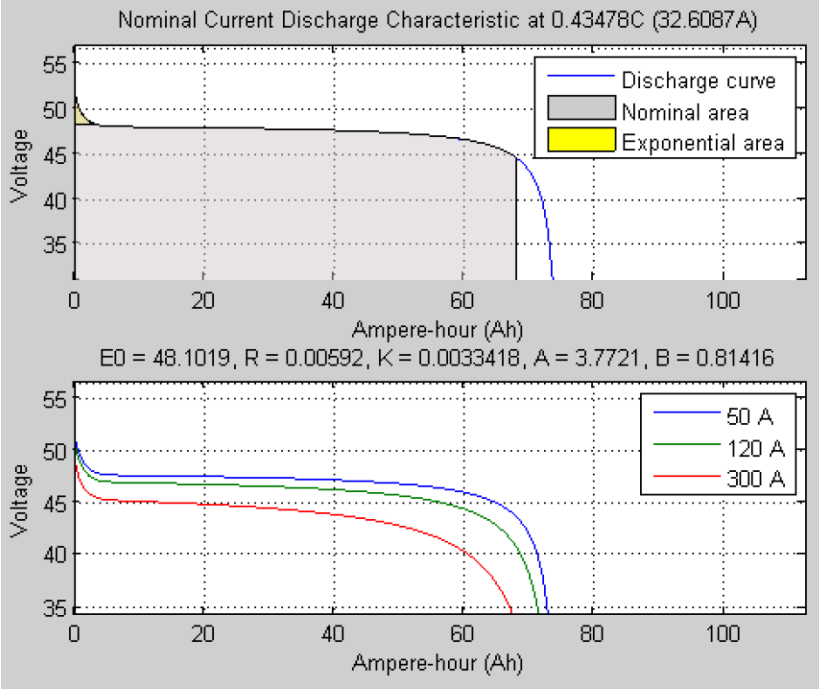

Figure 5 - Operational characteristic curves for 44.4V Battery module (single battery)

TABLE 3: Battery module parameters used in simulation analysis

Input parameters:	
Nominal Voltage	44.4 V
Rated capacity	90 Ah
Battery type	Lithium ion
Derived Parameters:	
Maximum Capacity	90 Ah
Fully Charged Voltage	51.2154 V
Nominal Discharge Current	32.6087 A
Internal Resistance	0.0058667 Ω
Capacity at Nominal Voltage	67.8261 Ah
Exponential Zone, Voltage	47.537 V
Exponential Zone, Capacity	3.68478 Ah
Battery Response Time	2-30 sec

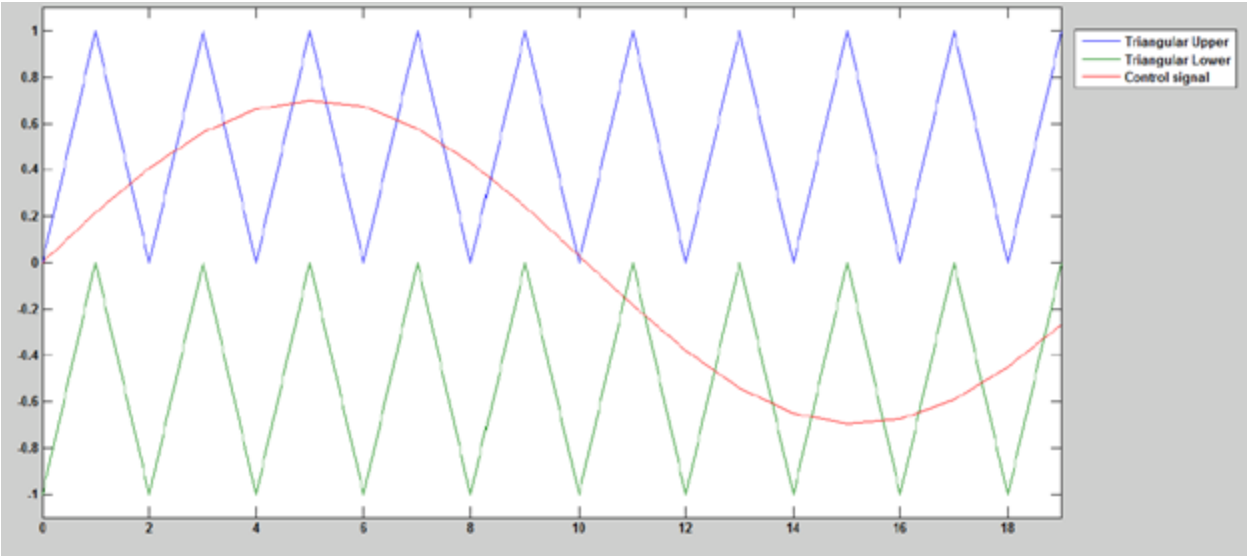

Figure 6 - Determination of switching pulses for the current control.

The current reference can be either positive or negative, indicating if the battery should charge or discharge. This implies that the bidirectional converter will have four operation modes depending on the current direction and which side is the HV or LV side. Switching operations for each of these situations are described in Table 4. For each of the four states in the table, one of the switches is named “leading”, which is the switch that decides the inductor current gain for that mode of operation.

Fig. 7 depicts the current control system implemented in Simulink software. Current is measured in the inductor placed at two DC sides and is compared with a reference current. The “repeating sequence” block in Simulink is used to make the two triangular signals. Each of these signals is compared separately with the PI controller output to define the gate signal for each of the switches S1 and S4. The signals for S1 and S3 are then inverted to produce the gate signals for S2 and S4, respectively.

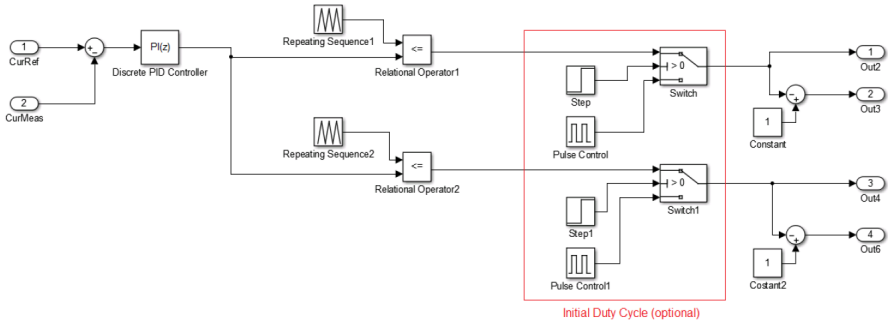

Figure 7 - Overview diagram of the current control strategy

TABLE 4: Switching logics of the battery in different operating conditions

Current Reference Status	Vbus > Vbattery	Vbattery > Vbus
Positive (Charge battery)	Buck mode S1 – Pulsing (leading) S2 – Pulsing S3 – On S4 – Off	Boost mode S1 – On S2 – Off S3 – Pulsing S4 – Pulsing (leading)
Negative (Discharge battery)	Boost mode S1 – Pulsing S2 – Pulsing (leading) S3 –On S4 – Off	Buck mode S1 – On S2 – Off S3 – Pulsing (leading) S4 – Pulsing

To avoid transients, there is a possibility to use a fixed duty cycle at the start of a simulation. This is controlled by the two logic switches, which will trip after a given time. The initial duty cycle is set as the expected resulting duty cycle and can be calculated from two following equations for buck mode (left equation) for boost mode (right side equation) [6].

$$d = \frac{V_{LV}}{V_{HV}} \qquad d = 1 - \frac{V_{LV}}{V_{HV}}$$

The proportional gain Kp mainly decides the response time of the controller, while the integral gain, Ki eliminates steady state error.

The model also includes a subsystem for measuring of duty cycles as shown in Fig. 8. The measured inputs for this subsystem are the gate pulses for switches S1 and S4. The integral of the input signals are divided by time to find the average duty cycle. The duty cycle measurement is only meant for measuring the average duty cycle in steady state.

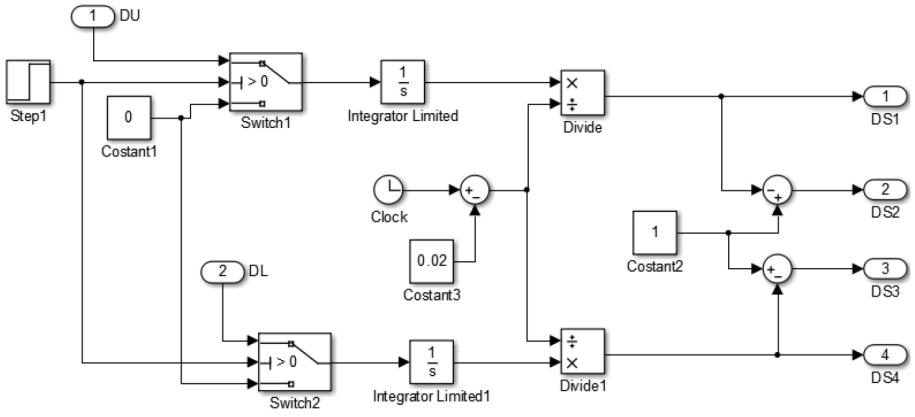

Figure 8 - Block diagram showing calculation of Duty Cycles and measurements

b) Voltage Control Strategy

The DC voltage of the bus is a common reference for loads and energy storage. The bus voltage can vary inside a range defined by two set points who will decide if the energy storage is to deliver or consume power from the system. The voltage control system will set the reference current for the converter based on measured bus voltage and SOC.

The purpose of the control loop shown in Fig. 9 is to compare the measured bus voltage with set points to determine when the battery should be charged or discharged. This means that the DC-link voltage can vary in a range, typically 880V-1050V, without the battery delivering or consuming power. If the voltage is inside this range, the input for the PI controller is set to zero. If the voltage is higher than the upper set point, or lower than the lower set point, the difference between that set point and the measured dc voltage will be the input signal for the PI controller. The saturation block in the model ensures that the current reference does not exceed maximum limits for the battery current. The battery's state of charge (SOC) is also measured and is an input variable in the control system. If the SOC is too high for the battery to consume power, or too low to deliver power, the maximum and minimum limits for the current are changed. Table 5 shows the strategy how SOC limits the output current reference, with typical values for both SOC and current. The PI controller can be tuned using the bisection method as an example. The voltage control should be slower than the current control, to avoid steps in the current reference.

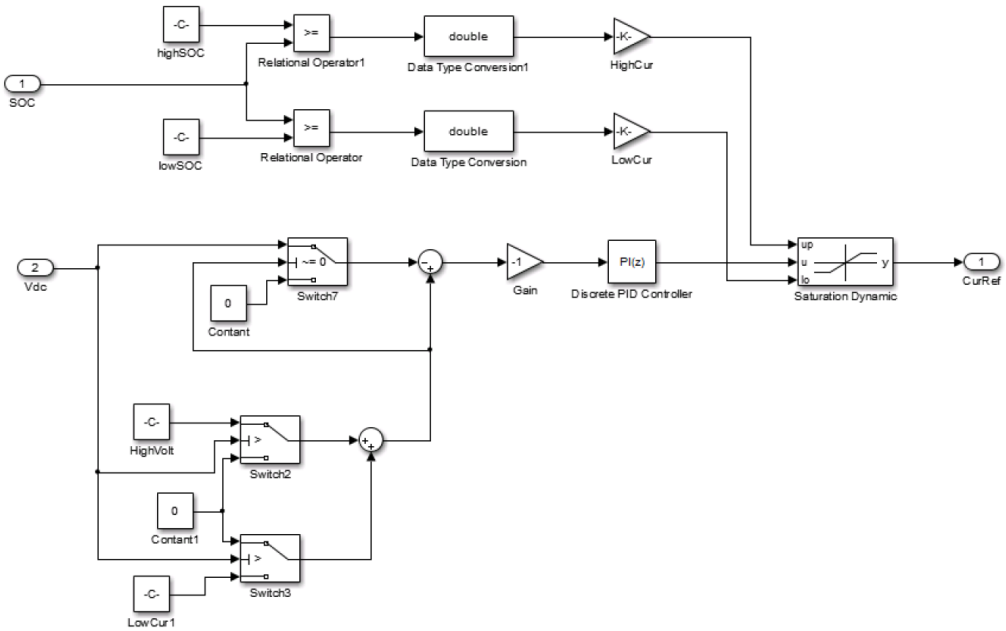

Figure 9 - A detailed voltage control block diagram

TABLE 5: Max and Min references for the current control loop considering the given SOC

SOC [%]	Imax	Imin
95-100	0	-110
65-95	110	-110
0-65	110	0

Battery DC-AC Inverter Structure and Its Control

The connected batteries interfaced to an Inverter which provides AC power to the connected busbar. A PWM closed-loop control is deployed with a carrier frequency of 4.8 kHz to generate gating pulses for the MOSFET power switches. To control the charge-discharge process of the battery energy storage including bidirectional DC-DC converter, the modulation indices are adjusted based on the difference angle between voltage and current measurements. However, the final gating pulses are determined through comparing sinusoidal PWM technique and direction of reference current.
A detailed inverter power stage and its control scheme presented in Fig. 10.

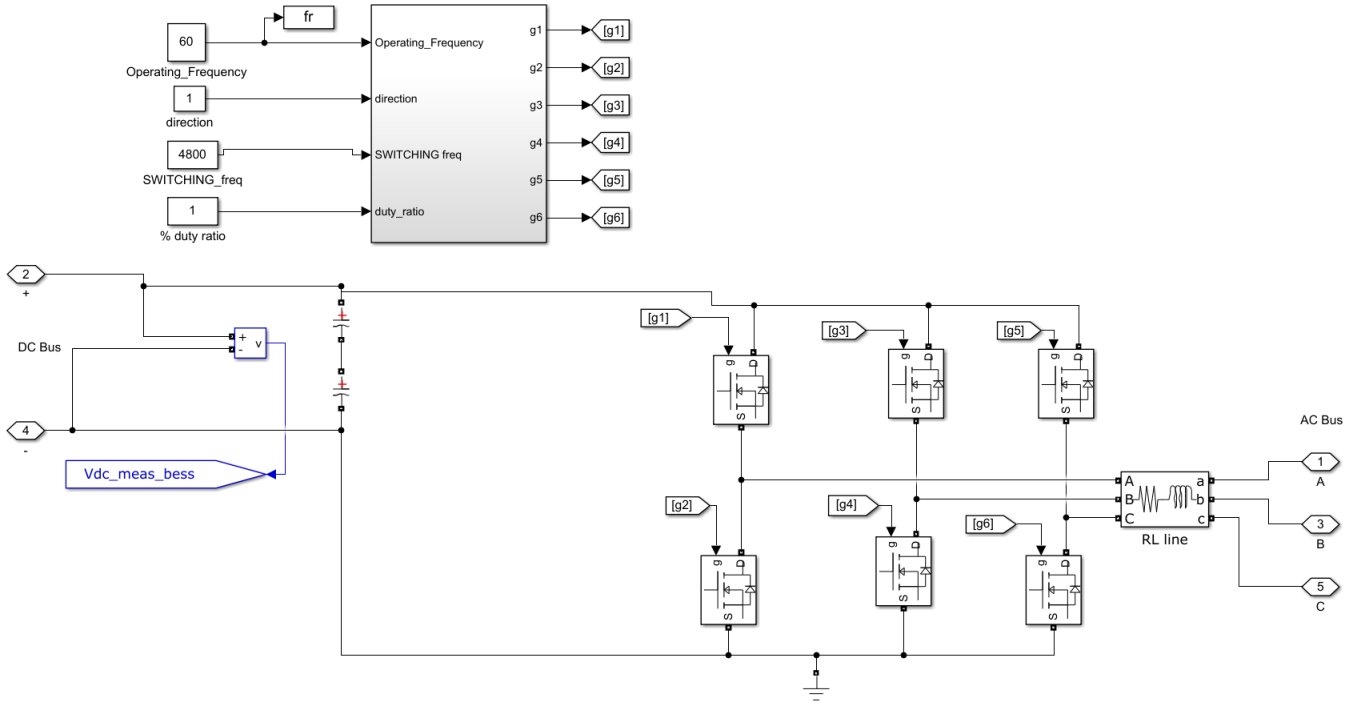

Figure 10 - BESS Inverter power stage configuration and its control

3.1.1.2 Solar PV Conversion Configuration and Its Control

The PV inverter equipped with IGBT bridge and its associated control scheme is shown in Fig. 11. A PV array available in Matlab/Simulink package is used to characterize performance of a solar panels from SunPower-SPR-415E [8]. Arrays operate with max power of 414.8 W, max power point voltage of 73V, total irradiance on the solar cells of 1000 W/m2 and a temperature of 25 Cdeg. A delta/star transformer is utilized to connect the PV inverter output to the 400 VAC busbar. A 3-level Sinusoidal PWM-controlled IGBT inverter with carrier frequency of 2.1 kHz operating via closed-loop control.

DC voltage control loop features with reference signal computed by MPPT algorithm based on widely used Perturb & Observe technique to be compared with the measured DC-link voltage. The output signal of this controller is then used for d-q current controller to generate reference voltage signal for PWM block to send gating pulses to IGBT power switches.

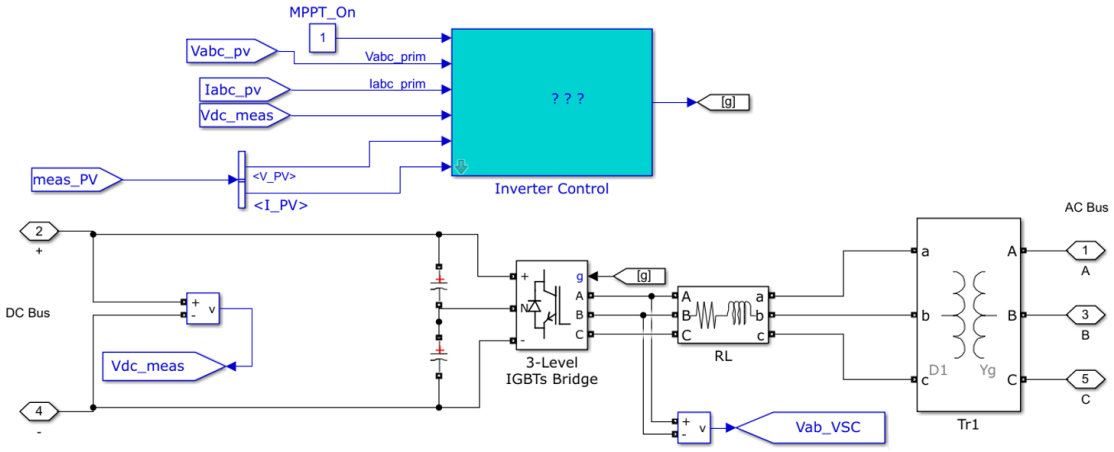

Figure 11 - PV inverter and its control

3.1.1.3 Diesel Generator and Its Configuration

The non-renewable generation of electrical power in the microgrid system is achieved by a 100kVA synchronous generator, driven by the Diesel Engine governor. The block available in Matlab is used for synchronous machine voltage regulator and exciter to implement the IEEE type AC1A excitation system model [9]. The output is the field voltage to apply to the Vf input of a Synchronous Machine block as shown in Fig. 12. This excitation system comprises by three sections. In the first part, the terminal voltage is compared against a reference and the error is fed to the regulator which is a first order system. This then goes through the exciter. The exciter

can incorporate a saturation function to account for magnetic core saturation and drop of exciter efficiency with loading.

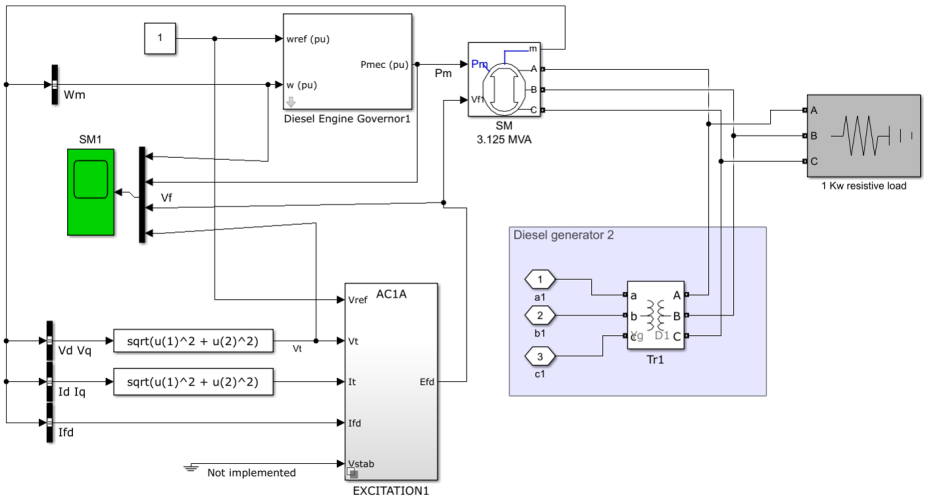

Figure 12 - Block diagram of the Diesel Generator and its control.

3.1.1.4 Type of Loads and Modeling

In the IEEE Microgrid model, the common 400VAC busbar interconnected to the common point of coupling is supplying different load types (e.g., Variable loads, DOL motor loads, VSD motor loads), which makes up a total load of 60 kW, with each load type having equal capacity, i.e., 20 kW. It should be mentioned that the original IEEE model includes ZIP load, while it has been replaced by variable load. The variable load is represented by a residential load model varying from 15 kW to 25 kW. The DOL motor load is represented by a fan load (Induction motor), and the VSD motor load to represent a pump load comprises Inverter controlled with space-vector modulation using switching frequency of 4.5kHz.
A direct online starter can only be used if the high inrush current of the motor does not cause an excessive voltage drop in the supply circuit. If a high voltage drop needs to be avoided, a star/delta starter should be used instead. DOL starters are commonly used to start small motors, especially 3 phase squirrel cage induction motors.

This model is useful to investigate the importance of the load characteristics and its effects for microgrid stability.
Fig. 13 shows the variable load and the VSD load models employed in the microgrid modeling work.

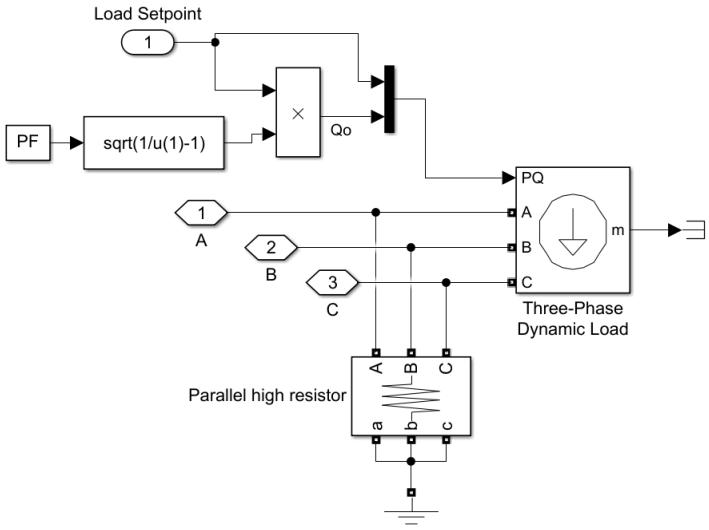

(a)

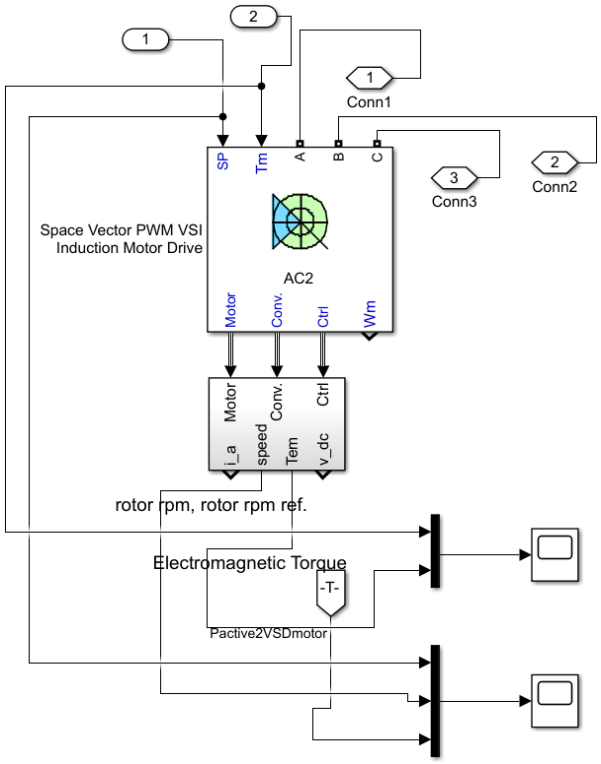

(b)

Figure 13 - A detailed block diagram of (a) Variable load; and (b) VSD motor load.

3.1.2 Case Studies and Performance Assessment

Several operating scenarios have been analyzed and the obtained results are evaluated to verify the acceptable performance of the microgrids and different subsystems. Fig. 14 illustrates real power measurement for Diesel Generator, Battery energy storage and solar PV system.
DC voltage reference tracking performance is compared with respective measured values for battery energy storage and PV system indicating a reasonable controller performance as shown in Fig. 15. In the case of BESS, a response time of 1min is assigned.

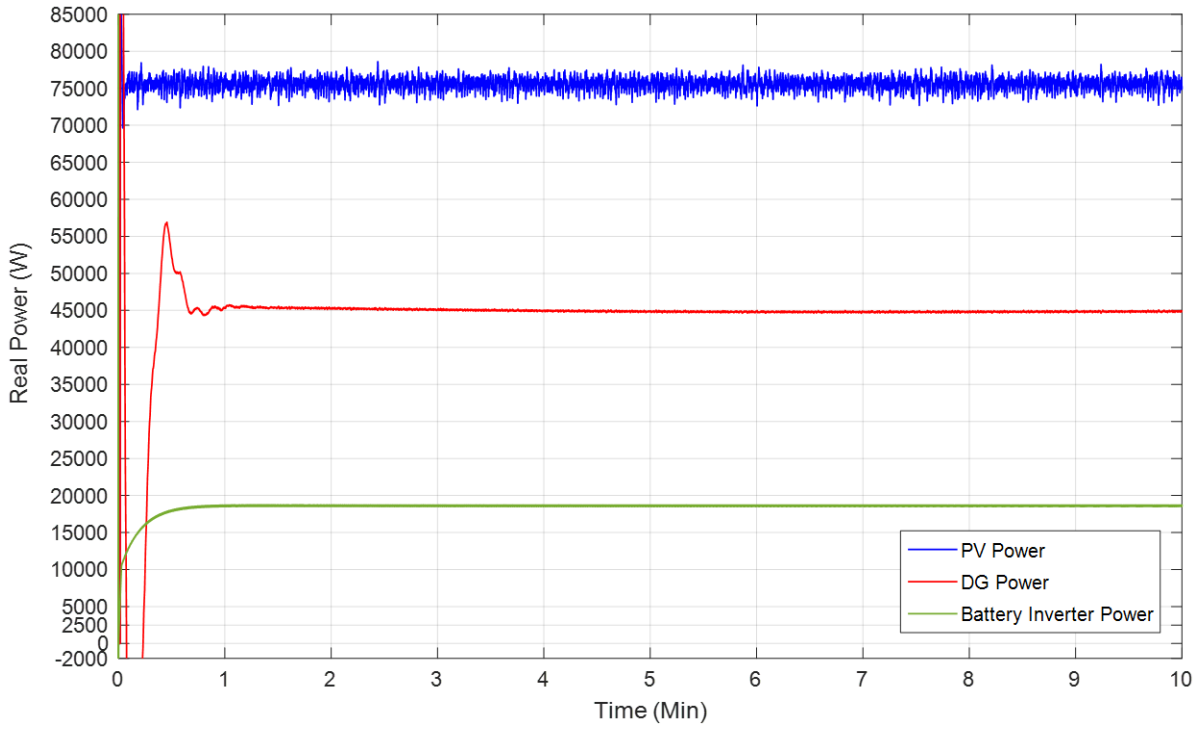

Figure 14 - Active power measurements in various distributed generation resources.

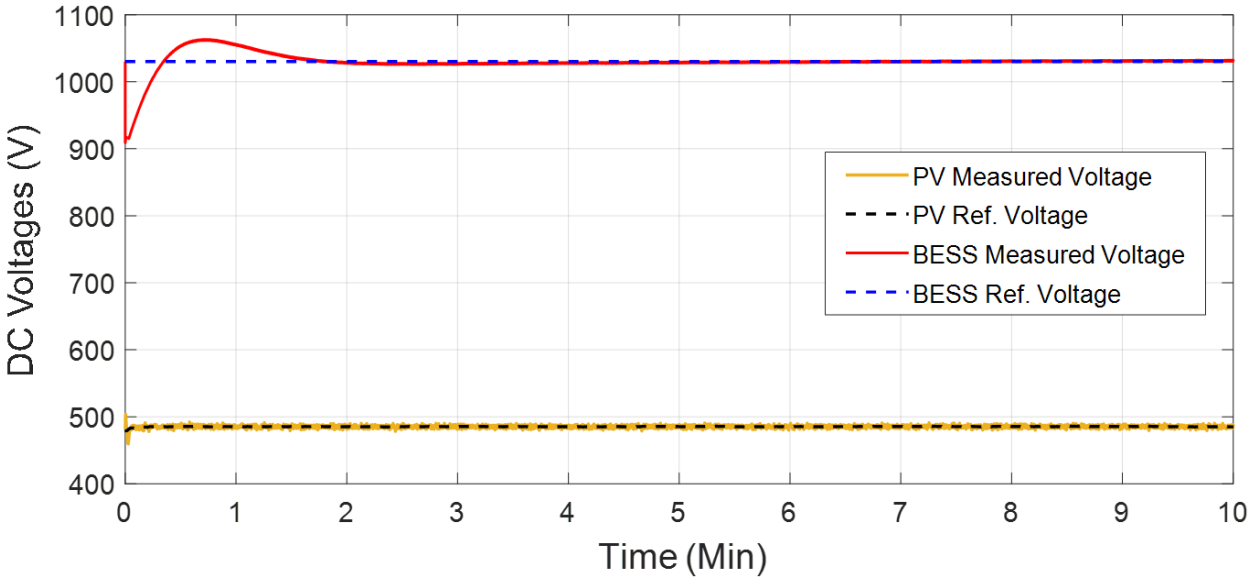

Figure 15 - DC voltage reference tracking performance for Battery Energy storage and PV Systems (BESS voltage reference=1030V, PV DC voltage reference=480V)

Fig. 16 provides a measured typical waveforms for a battery pack which includes 4 single batteries with operating characteristics given in Fig. 5.

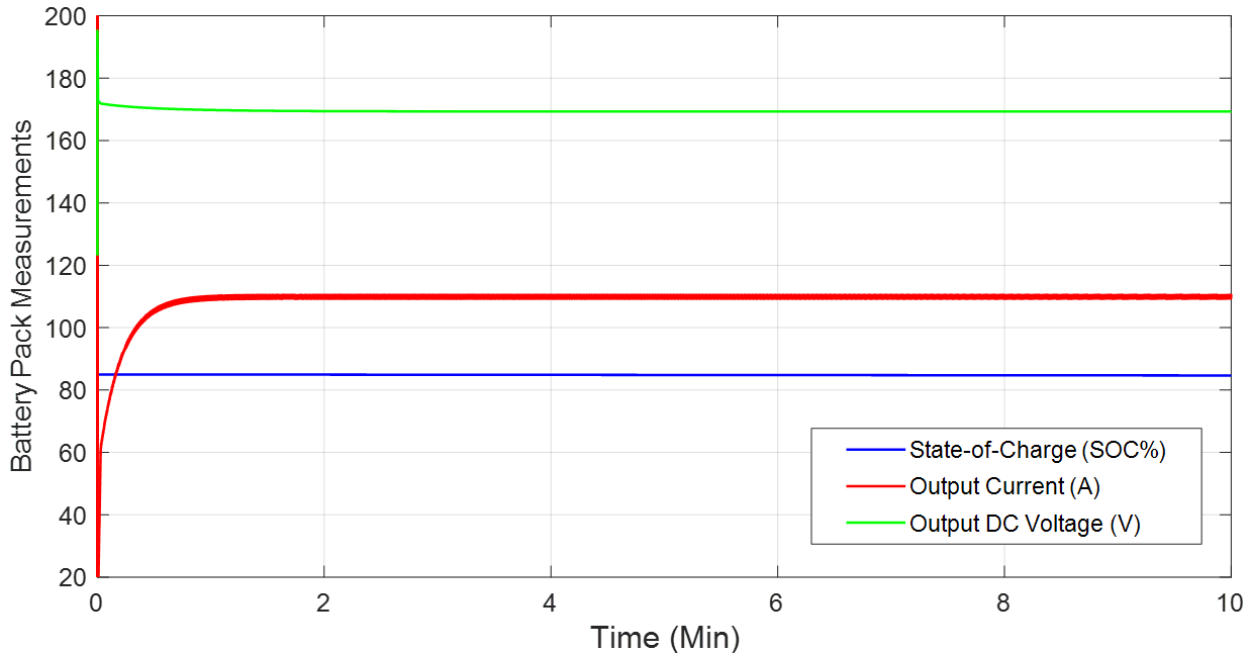

Figure 16 - Operating waveforms of battery energy storage during charging mode.

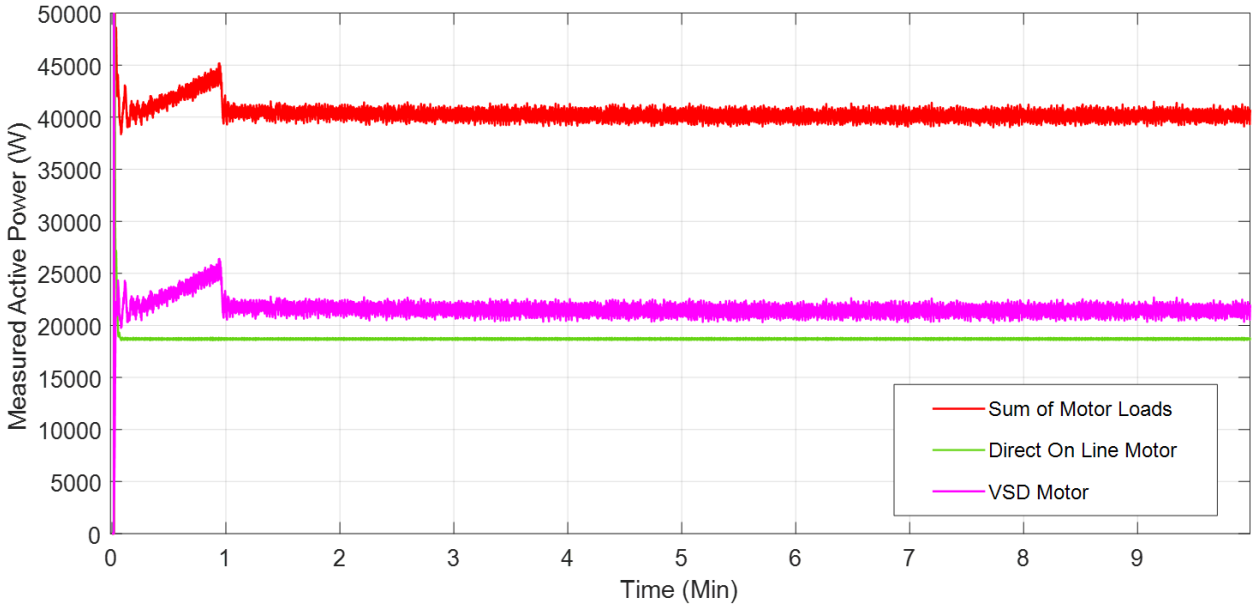

Figure 17 - Active power measurements in motor loads.

From a motor load perspective, it is important to achieve their nominal power in normal working conditions. The real power measurements for DOL and VSD loads are shown in Fig. 17.

Another testing scenario is carried out to reflect performance of the entire system with respect to dynamic operating condition. Therefore, the operating scenario is applied when DG is disconnected at t=4 min, and VSD motor torque is increased by 50% from 11 n.m to 16.5 n.m at t=7min. VSD torque and speed measurements are compared with reference values as presented in Figs. 18 and 19. Note that the rotor speed reference is ramped up from start-up til 1 min to reach a nominal value of 1700RPM.

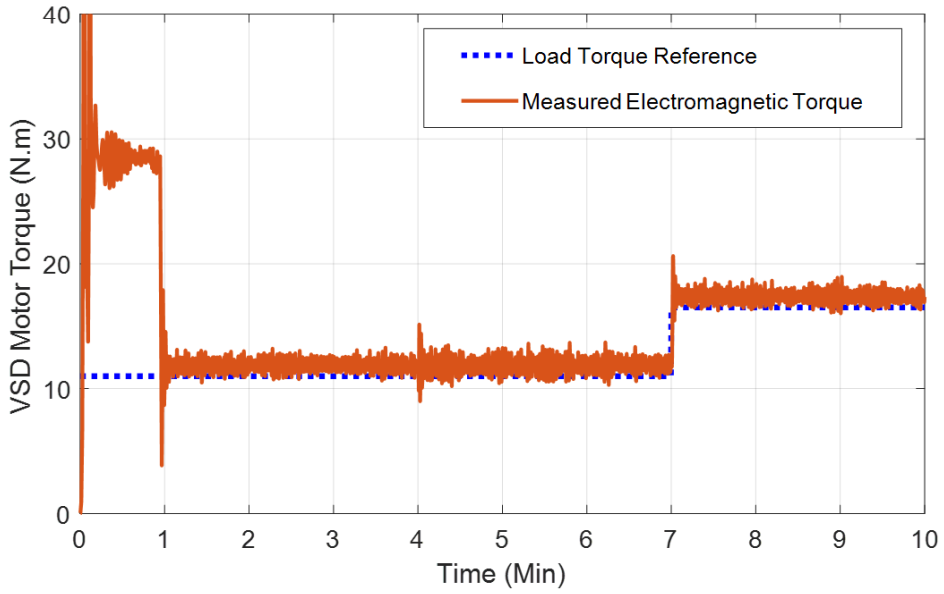

Figure 18 - Reference torque tracking in VSD motor load when DG disconnected at t=4 min and motor torque increased by 50% at t=7min.

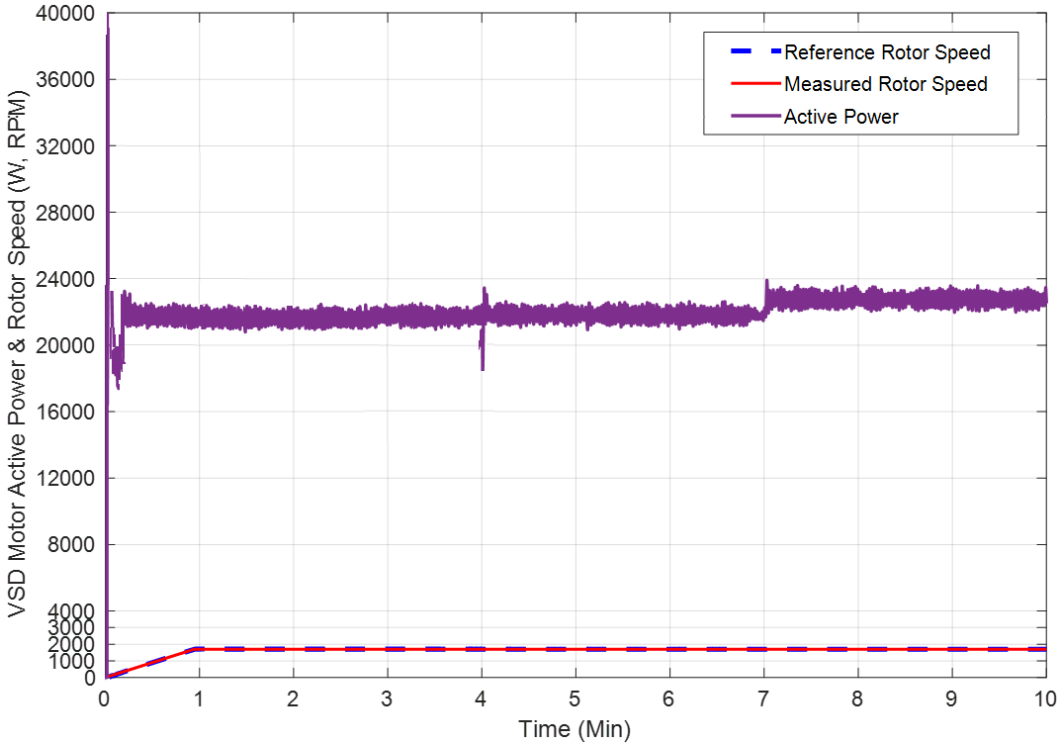

Figure 19 - Measured active power and rotor speed tracking for VSD motor when DG disconnected at t=4min and motor torque increased by 50% at t=7min..

The SOC curve during battery discharging mode is shown in Fig. 20. Diesel generator mechanical speed, power and stator terminal voltage are depicted in Fig. 21.

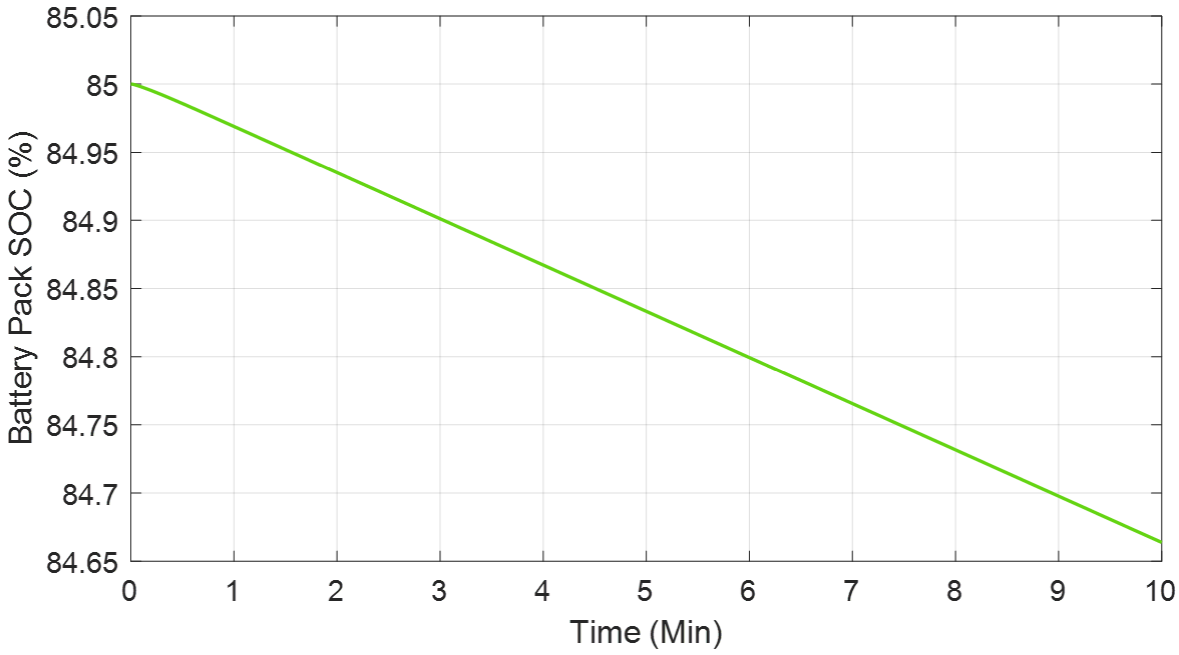

Figure 20 - State-of-the-charge in percentage for the battery during discharging operation.

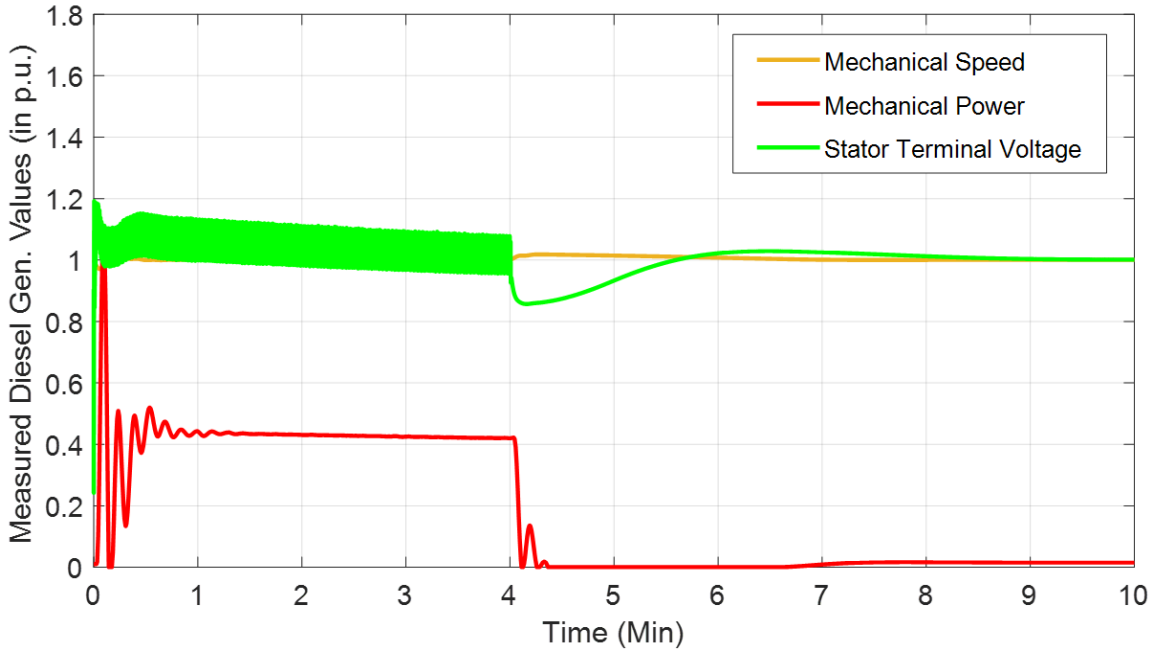

Figure 21 - Obtained waveforms from diesel generator measurements when DG disconnected at t=4 min and motor torque increased by 50% at t=7min..

References

[1] National Renewable Energy Laboratory, “IEEE 1547 and 2030 Standards for Distributed Energy Resources Interconnection and Interoperability with the Electricity Grid, December 2014.

[2] EPRI, “The Integrated Grid, Phase II: The Development of a Benefit-Cost Framework,” Palo Alto, CA, USA, June 2014.

[3] IEEE PES Task Force on Microgrid Stability Analysis and Modeling, “TR66: Microgrid Stability Definitions, Analysis, and Modeling,” June 2018.

[4] Y. Yang, P. Enjeti, F. Blaabjerg, H, Wang, “Wide-Scale Adoption of Photovoltaic Energy: Grid Code Modifications Are Explored in the Distribution Grid,” *IEEE Industry Applications Magazine,* vol. 21, no. 5, pp. 21-31, Sept./Oct. 2015

[5] H. Xiao, “Overview of Transformerless Photovoltaic Grid-Connected Inverters,” *IEEE Transactions on Power Electronics,* Early Access, no. 99, pp. 1-1, Jun. 2020

[6] Ned Mohan, Tore Undeland, William Robins, ‘’Power Electronics- Converters, Applications, and Design’’, John Wiley & Sons, Inc., 2003.

[7] Energy Corvus, “Data sheet for AT6500,” Available: http://www.corvus-energy.com/pdf/AT6500_Data_Sheet_2_page.pdf

[8] http://www.solarhub.com/product-catalog/pv-modules/4197-SPR-415E-WHT-D-SunPower

[9] IEEE Std. 421.5-2005, “IEEE Recommended Practice for Excitation System Models for Power System Stability Studies,” 2006.

[10] OPAL-RT Technologies. Available at: https://www.opal-rt.com

[11] Typhoon HIL, Available at: https://www.typhoon-hil.com/

[12] dSPACE HIL Testing System, Available at: https://www.dspace.com/en/inc/home/products/systems/ecutest.cfm

[13] M. Ilièes Ayachi, S. Ahmed, and **L. Vanfretti**, “A PM-Based Machine Learning Application for Fast Detection of Wind Farm Oscillations from Wind Farms,” 2019 Saudi Arabia Smart Grid (SASG 2019), 10-12 December 2019, Ritz Carlton Hotel, Jeddah, Saudi Arabia.

[14] https://drive.google.com/drive/folders/1XXGn-ZAw3w_5J2_-rszfhP75HDlOb_xi

[15] M. I. Ayachi, L. Vanfretti, S. Ahmed “A PMU-Based Machine Learning Application for Fast Detection of Forced Oscillations from Wind Farms,” Summer 2019.

[16] https://drive.google.com/drive/folders/1Emd8y0mvPgvQAySngBAn2zgcxAjJcBPn

[17] “Jetson Nano: Deep Learning Inference Benchmarks”, Available: https://developer.nvidia.com/embedded/jetson-nano-dl-inference-benchmarks

Appendix